Nanoscale

ROYAL SOCIETY OF CHEMISTRY

PAPER

View Article Online
View Journal | View Issue

Cite this: *Nanoscale*, 2020, **12**, 6096

Synthesis of gadolinium/iron–bimetal–phenolic coordination polymer nanoparticles for theranostic applications†

Jing Qin,‡[a] Guohai Liang,‡[b] Youyou Feng,[a] Bingxi Feng,[a] Gen Wang,[a] Na Wu,[a] Yongxi Zhao [a] and Jing Wei *[a]

Received 25th November 2019,
Accepted 9th February 2020

DOI: 10.1039/c9nr10020b

rsc.li/nanoscale

Integration of diagnostic and therapeutic components into a single coordination polymer nanoparticle is desirable for theranostic applications, but still challenging. Herein, we report the synthesis of bimetal–phenolic coordination polymer nanoparticles using gadolinium nitrate and ferrous sulphate as a metal source, and plant polyphenols (*i.e.*, tannic acid) as an organic ligand *via* a metal–catechol coordination assembly process. Such coordination polymers show a tunable molar ratio of Gd/Fe and high dispersibility and stability in aqueous solution. The coordination polymers reveal composition-dependent performance for longitudinal relaxivity and photothermal conversion. The longitudinal relaxivity is positively related to the molar ratio of Gd/Fe, while the photothermal performance is negatively related to the molar ratio of Gd/Fe in the coordination polymers. The coordination polymers with an optimized molar ratio of Gd/Fe exhibit an ultra-small hydrodynamic diameter (~23 nm), a high r_1 value (9.3 mM^{-1} s^{-1}) with low r_2/r_1 (1.26) and high photothermal conversion efficiency (η = 37%). They can be used as a contrast agent for T_1-weighted magnetic resonance imaging of EMT-6 tumor bearing mice, which can effectively enhance the signals of tumors. They can also effectively suppress tumor growth *via* photothermal therapy. This work brings new insights for the synthesis of multifunctional coordination polymer nanoparticles and extending their potential applications in theranostics.

1. Introduction

Magnetic resonance imaging (MRI) has become an attractive technique in modern diagnostic medicine using an external magnetic field, radio waves and a computer to generate high-quality three-dimensional images of soft tissue.[1–10] This technique is noninvasive, and does not require ionizing radiation which may cause harmful side effects. Moreover, MRI shows a high spatial resolution, and an almost limitless tissue penetration depth. Consequently, it has been widely used for the diagnosis of different diseases. Signal intensity in MRI is related to the relaxation rate of *in vivo* water protons and can be enhanced by the administration of a contrast agent (CA) prior to scanning.[4,5] Thus, in clinical MRI, about 30% of the patients need to be injected with a CA to enhance the contrast between their normal and pathological tissues.[4] Gadolinium containing complexes have been widely used as a CA due to their high magnetic moment and long electron spin relaxation time. However, the commonly used low-molecular-weight Gd complexes (such as Magnevist) show drawbacks such as short circulation time in the body, low longitudinal relaxivity (r_1), no specificity to tumors and single function, which inevitably hinders their potential application for multimodal imaging and theranostics.

Photothermal therapy (PTT) has been regarded as a powerful technique for cancer treatment due to its high selectivity and minimal invasiveness.[11–13] Its therapeutic effects only occur at the tumor sites with both photothermal therapeutic agent accumulation and localized near-infrared (NIR) laser exposure, which can effectively lower the risk of damage to normal tissue. Thus, development of multifunctional theranostic nanoplatforms with improved diagnostic sensitivity by MRI and therapeutic efficiency of tumors through PTT is desirable but challenging.

Recently, nanoscale coordination polymers (CPs) constructed using metal ion/clusters and organic ligands have attracted extensive attention due to their intrinsic biodegrad-

[a]*The Key Laboratory of Biomedical Information Engineering of Ministry of Education, School of Life Science and Technology, Xi'an Jiaotong University, Xi'an, Shaanxi 710049, P. R. China. E-mail: jingwei@xjtu.edu.cn*
[b]*College of Biophotonics, South China Normal University, Guangzhou 510631, P. R. China*

†Electronic supplementary information (ESI) available. See DOI: 10.1039/c9nr10020b

‡These authors contributed equally to this work.

ability, tunable structure and composition, and easy surface modification, as well as tailorable size at the nanoscale.[14–18] Therefore, nanoscale CPs have been widely used for medical imaging, sensing, and therapy, especially for multimodal imaging and theranostics, which are highly required for accurate medicine applications. Due to the diversities of organic ligands, various kinds of nanoscale CPs have been synthesized. Metal–phenolic coordination polymers (MPCPs), as one kind of CP, are usually constructed using plant polyphenols as an organic ligand.[19–21] Plant polyphenols are one of the nature abundant resources, which can be used for antimicrobial, antioxidant and radical scavenging. Moreover, plant polyphenols can chelate with various metal ions *via* a metal–catechol coordination bond to form MPCPs. As a result, MPCPs exhibit metal-dependent properties and have recently attracted increasing interest in sensing, biomedical imaging, drug delivery and therapy.[22–47] For example, iron–phenolic coordination polymers have been recently investigated for PTT due to their high photothermal conversion efficiency induced by a strong ligand-to-metal charge transfer band.[39–41,48] However, they usually show low longitudinal relaxivity (r_1) or can only be used for T_2-weighted MRI. Gd–Phenolic coordination polymers could be potentially used for T_1-weighted MRI.[24] However, the photothermal conversion performance and MRI *in vivo* of Gd–phenolic coordination polymers are not investigated yet. Generally, the nanoscale MPCPs fail to integrate the functions of highly efficient T_1-weight MRI and PTT. It is anticipated that bimetal (such as Gd, Fe)–phenolic coordination polymer nanoparticles would effectively integrate the advantages of Fe- and Gd-based coordination polymers and exhibit high therapeutic efficiency for T_1-weighted MRI and PTT.[40,49–51] However, the complicated metal (*i.e.* Fe and Gd)–ligand coordination assembly process and unavoidable oxidation induced self-polymerization of polyphenols severely hinder the controllable synthesis of bimetal–phenolic coordination polymers with an ultra-small diameter and tunable physicochemical properties. To the best of our knowledge, the controllable synthesis of Gd/Fe–bimetal–phenolic coordination polymer nanoparticles with tailorable compositions and size and their therapeutic performance have never been investigated.

Herein, Gd/Fe–bimetal–phenolic coordination polymer nanoparticles were synthesized for the first time *via* a controllable metal–catechol coordination assembly process using gadolinium nitrate and ferrous sulphate as a metal source and plant polyphenols (such as tannic acid, TA) as a ligand (Fig. 1a). The molar ratio of Gd/Fe in the coordination polymers was positively correlated with the molar ratio of the Gd/Fe precursor. When the molar ratio of Gd/Fe increased, the longitudinal relaxivity (r_1) of coordination polymers increased while the photothermal performance decreased. By optimizing the molar ratios of Gd/Fe in CPs, the obtained bimetal–phenolic coordination polymers exhibited an ultra-small hydrodynamic diameter (~23 nm), high colloidal stability, a high r_1 value (9.3 mM^{-1} s^{-1}) with low r_2/r_1 (1.26) and high photothermal conversion efficiency (η = 37%). Such CPs were further used for T_1-weighted MRI of tumors *in vivo*, which can effectively enhance the MR signals. They can also effectively suppress tumor growth *via* photothermal therapy.

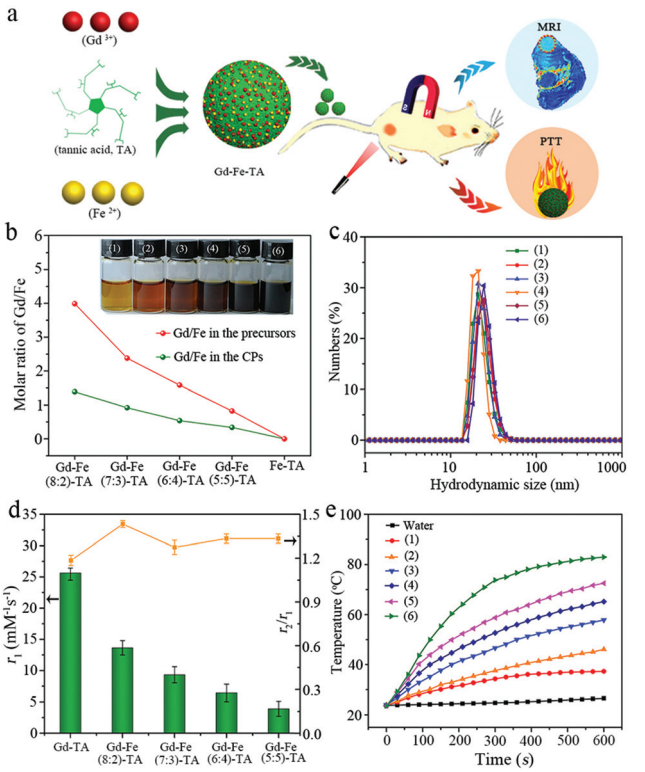

Fig. 1 (a) Schematic illustration of the synthesis and theranostic applications of bimetal–phenolic coordination polymer nanoparticles. (b) The molar ratios of Gd/Fe in the metal precursors and CPs. The inset in (b) shows the photographs of CPs with different Gd/Fe ratios in aqueous solution. (c) The hydrodynamic size distributions of CPs with different Gd/Fe ratios measured by DLS. (d) r_1 and r_2/r_1 values for different CPs. (e) Time-dependent temperature change curves of different CP solutions (1.0 mg mL^{-1}) upon exposure to the 808 nm NIR laser at a power density of 1.0 W cm^{-2}. The samples in b, c and e were (1) Gd–TA, (2) Gd–Fe(8 : 2)–TA, (3) Gd–Fe(7 : 3)–TA, (4) Gd–Fe(6 : 4)–TA, (5) Gd–Fe (5 : 5)–TA and (6) Fe–TA, respectively.

2. Results and discussion

2.1. Synthesis and characterization of Gd/Fe–bimetal–phenolic coordination polymer nanoparticles

Gd/Fe–bimetal–phenolic coordination polymer nanoparticles were synthesized using gadolinium nitrate and ferrous sulphate as a metal source and tannic acid (TA) as an organic ligand under alkaline conditions. TA firstly reacted with formaldehyde under alkaline conditions to form tannic acid-formaldehyde oligomers.[52] The hydrodynamic size of the tannic acid-formaldehyde oligomers was around 9.5 nm after reaction for 12 hours (Fig. S1†). The metal sources were then added, and the metal species can further crosslink the tannic acid-formaldehyde oligomers *via* a metal–catechol coordination bond.[30] The hydrodynamic size of metal–polyphenol–formaldehyde nanoparticles further increased to 23.2 nm after

24 hours, indicating the formation of metal-organic coordination polymers. After further hydrothermal treatment, dialysis and freeze drying, the bimetal–phenolic coordination polymers were obtained, which were denoted as Gd–Fe($x:y$)–TA ($x:y$ refers to the molar ratio of Gd/Fe in the precursor). When Gd or Fe ions were used solely, the obtained CPs were denoted as Gd–TA or Fe–TA.

Photographs of Gd–TA, Fe–TA and Gd–Fe($x:y$)–TA aqueous solution revealed that such CPs could be well dispersed in water (Fig. 1b). The colour of Gd–TA CPs was light yellow. When the molar ratio of Gd/Fe in the precursors decreased, the colour of the Gd–Fe($x:y$)–TA CP solution turned darker gradually. Fe–TA solution showed black colour. The Gd and Fe contents in Gd–Fe($x:y$)–TA coordination polymers were determined by inductively coupled plasma mass spectrometry (ICP-MS). The Gd contents in the CPs for Gd–TA, Gd–Fe(8 : 2)–TA, Gd–Fe(7 : 3)–TA, Gd–Fe(6 : 4)–TA, and Gd–Fe(5 : 5)–TA were 74, 58, 49, 43 and 31 mg g^{-1} respectively. The Fe contents in the CPs for Gd–Fe(8 : 2)–TA, Gd–Fe(7 : 3)–TA, Gd–Fe(6 : 4)–TA, Gd–Fe(5 : 5)–TA and Fe–TA were 15, 19, 28, 32 and 83 mg g^{-1} respectively. Generally, the contents of Gd and Fe in the CPs were positively related to the amount of metal precursor (Table S1†). When the molar ratio of Gd/Fe in the metal precursor increased, the molar ratio of Gd/Fe in the CPs increased (Fig. 1b). The molar ratios of Gd/Fe for Gd–Fe(8 : 2)–TA, Gd–Fe(7 : 3)–TA, Gd–Fe(6 : 4)–TA and Gd–Fe(5 : 5)–TA were 1.39, 0.92, 0.54 and 0.34 respectively. The molar ratio of Gd/Fe in the CPs was slightly lower than that in the precursor, suggesting that Gd(III) had a weaker chelation ability with polyphenols than Fe (II). The hydrodynamic diameter of MPCPs with different molar ratios of Gd/Fe was in the range of 20–30 nm, indicating that the molar ratios of Gd/Fe cannot obviously affect the diameter of the CPs (Fig. 1c, Table S2†). The zeta potentials of MPCPs were in the range of −2.76 to −5.66 mV.

In order to synthetically evaluate the MRI performance of MPCPs with different compositions, the longitudinal relaxivity (r_1) and transverse (r_2) relaxivity of these CPs with different ratios of Gd/Fe were further measured (Fig. 1d). The longitudinal relaxivity increased from 3.9 to 13.6 mM^{-1} s^{-1} when the molar ratio of Gd/Fe in the metal precursors increased from 5 : 5 to 8 : 2. The longitudinal relaxivity for Gd–TA was as high as 25.9 mM^{-1} s^{-1}. The value of r_2/r_1 remained nearly constant in the range of 1.2–1.4, indicating that such materials could be used as a T_1 contrast agent. Then, MPCPs with different molar ratios of Gd/Fe were dispersed in water and irradiated by an 808 nm laser. The temperature of all the MPCP solutions increased dramatically under irradiation when compared with pure water (Fig. 1e). The final temperatures of the MPCP solution after irradiation for 10 min were 37.3, 46.1, 58.4, 65.2, 72.5, and 82.9 °C for Gd–TA, Gd–Fe(8 : 2)–TA, Gd–Fe(7 : 3)–TA, Gd–Fe(6 : 4)–TA, Gd–Fe(5 : 5)–TA and Fe–TA, respectively. By contrast, the final temperature of pure water under irradiation was 28.1 °C, which was a little higher than the initial temperature (23.8 °C). The increase of the solution temperature for MPCPs with different compositions was different. The final temperature was mainly dependent on the molar ratio of Gd/Fe. A higher molar ratio of Gd/Fe leads to a lower final temperature. The UV-vis-NIR absorption spectra of MPCP solution showed a broad peak at around 565 nm, which was ascribed to the coordination between Fe ions and polyphenols (Fig. S2†).[53] Moreover, when the iron contents in the coordination polymers increased, the absorbance of coordination polymers at 808 nm also increased. Based on the above results, the longitudinal relaxivity of MPCPs was positively related to the molar ratio of Gd/Fe, while their photothermal performance was negatively related to the molar ratio of Gd/Fe. By comprehensive consideration of the performance of bimetal–phenolic coordination polymers, Gd–Fe(7 : 3)–TA was selected as an integrated nano-platform for the application of MRI and PTT.

Before investigation of the biomedical application of bimetal–phenolic coordination polymers, the physicochemical properties of Gd–Fe(7 : 3)–TA were further studied. Gd–Fe (7 : 3)–TA in water (1.0 mg mL^{-1}) showed a clear solution, indicating a good dispersity (Fig. S3†). After standing at room temperature for 30 days, no significant aggregation was observed in the solution. The hydrodynamic diameter of Gd–Fe(7 : 3)–TA was centered at 22.5 nm. After 30 days, the hydrodynamic size of Gd–Fe(7 : 3)–TA remained nearly unchanged (23.1 nm), indicating that Gd–Fe(7 : 3)–TA nanoparticles showed high colloidal stability in water (Fig. 2a). Moreover, Gd–Fe(7 : 3)–TA displayed excellent hydrophilicity and stability in different buffers with a similar hydrodynamic size (Fig. S4 and Table S3†). The transmission electron microscopy (TEM) image of Gd–Fe(7 : 3)–TA exhibited spherical nanoparticles (Fig. 2b). The diameter of Gd–Fe(7 : 3)–TA calculated from TEM images was around 25 nm (Fig. S5†). The atomic force microscopy (AFM) image of Gd–Fe(7 : 3)–TA further revealed that the polymers were nanoparticles with a diameter around

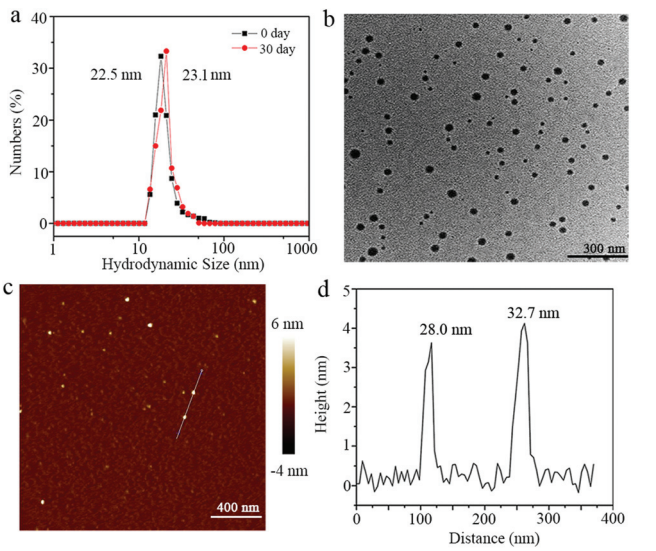

Fig. 2 (a) The hydrodynamic size distributions of Gd–Fe(7 : 3)–TA at 0 day and 30 days measured by DLS. (b) TEM image and (c) AFM image of Gd–Fe(7 : 3)–TA. (d) The height profile along the line marked in the AFM image.

28.0 and 32.7 nm (Fig. 2c and d), which is consistent with TEM and DLS results. The X-ray diffraction (XRD) patterns of Gd–Fe(7 : 3)–TA revealed an amorphous structure (Fig. S6†). The existence of Fe and Gd in the Gd–Fe(7 : 3)–TA CPs was further confirmed by X-ray photoelectron spectroscopy (Fig. S7†). The Gd 4d spectrum showed two peaks at 1220 and 1187 eV. The Gd 3d spectrum exhibited two peaks at 142 and 148 eV. These peaks suggested the formation of Gd–O bonds in the coordination polymers.[54] The Fe $2p_{3/2}$ spectrum revealed a broad peak in the range of 705–718 eV, indicating the existence of Fe(II) and Fe(III).[55] The existence of Fe(III) may be due to the oxidation of Fe(II)–TA compounds by the oxygen from air.[56,57] The Fe(III) species in the coordination polymers can also show longitudinal relaxivity, which will further affect the contrast effect of Gd–Fe–TA coordination polymers.

2.2. MRI performance

The longitudinal relaxivity (r_1) and transverse (r_2) relaxivity for Gd–Fe(7 : 3)–TA were 9.3 and 11.8 mM^{-1} s^{-1} respectively (Fig. 3a). The r_2/r_1 value was 1.26, suggesting that Gd–Fe(7 : 3)–TA could be used as an efficient contrast agent for T_1-weighted MR imaging. The r_1 value was 2.5 fold higher than that of Gd–DTPA (3.7 mM^{-1} s^{-1}) measured under the same conditions (Fig. 3a). The r_1 value was also higher than that of the majority of metal–polyphenol composites (Table S4†). To further evaluate the MRI contrasting ability, T_1-weighted MR images of Gd–Fe (7 : 3)–TA aqueous solution with different concentrations of Gd were collected using a 1.0 T MRI scanner (Fig. 3c). It was observed that MR signal intensity was positively correlated with the concentrations of Gd ions. Gd–Fe(7 : 3)–TA showed higher signal intensity than Gd–DTPA at the same Gd concentration. Such results demonstrated its potential application in MRI.

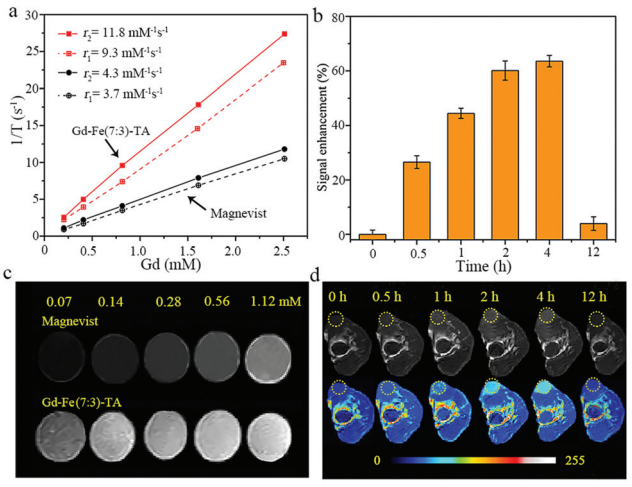

Fig. 3 (a) Plots of $1/T_1$ and $1/T_2$ over the concentrations of Gd in Gd–Fe (7 : 3)–TA and Magnevist (Gd–DTPA). (b) The quantification of signal enhancement for tumors after intravenous injection of Gd–Fe(7 : 3)–TA at different time intervals. (c) Magnetic resonance image of Gd–Fe (7 : 3)–TA and Magnevist with different concentrations of Gd. (d) *In vivo* T_1-weighted magnetic resonance images of mice bearing EMT-6 tumors after intravenous injection of Gd–Fe(7 : 3)–TA at different time intervals.

The leakage of toxic Gd ions in the CPs was one of the main problems for Gd-based CPs due to their small size and unstable framework. The leakage experiment of metal ions for Gd–Fe(7 : 3)–TA was conducted by dialyzing against different solvents (Fig. S8†). The residual Gd in Gd–Fe(7 : 3)–TA was 80% (in water) and 82% (in PBS) after dialysis for 96 hours. They also exhibited high stability under weakly acidic conditions (pH = 6.5 and 5.8). The covalent crosslink of polyphenol ligands by formaldehyde under alkaline conditions and hydrothermal treatment will lead to a dense polymer framework and increase the stability of coordination polymers. Because free Gd ions are toxic, such good stability of Gd–Fe(7 : 3)–TA is beneficial for their application *in vivo*.

The MRI performance of Gd–Fe(7 : 3)–TA *in vivo* was further investigated. All animal procedures were performed in accordance with the Guidelines for Care and Use of Laboratory Animals of South China Normal University and approved by the Animal Ethics Committee of South China Normal University. EMT-6 tumor bearing mice were injected with Gd–Fe(7 : 3)–TA solution (4 mg kg^{-1}) *via* the tail vein and placed in a 1.0 T MRI scanner. It was obvious that the MR image in the tumor region gradually brightened over time (Fig. 3d). The highest relative signal enhancement (RES) in tumors was 63.5 ± 2.5% at 4 h after intravenous injection (Fig. 3b). These experimental results indicated that Gd–Fe(7 : 3)–TA could effectively enhance MR signals in the region of tumors through the enhanced permeability and retention effect.

2.3. PTT performance

Gd–Fe(7 : 3)–TA solution exhibited broad absorption ranging from the ultraviolet to NIR region (Fig. S9†). The absorption of Gd–Fe(7 : 3)–TA solution at 808 nm was linearly correlated with the concentration of Gd–Fe(7 : 3)–TA solution. The strong NIR absorption of Gd–Fe(7 : 3)–TA makes it a promising agent for photothermal applications. Gd–Fe(7 : 3)–TA solution was irradiated with an 808 nm laser. Pure water was used as a negative control. The temperature changes of Gd–Fe(7 : 3)–TA solution were recorded by using a digital thermometer and an infrared thermal camera (Fig. 4a and b and Fig. S10†). After irradiation for 10 min, the temperature of Gd–Fe(7 : 3)–TA solution increased from 23.8 °C to 58.4 °C at a concentration of 1.0 mg mL^{-1}. When the concentration of Gd–Fe(7 : 3)–TA solution was 0.5, 0.75, and 1.5 mg mL^{-1}, the final temperature was 37.6, 44.7, and 63.2 °C respectively. When Gd–Fe(7 : 3)–TA solution (1.0 mg mL^{-1}) was exposed to the NIR laser irradiation with a power density of 1.0, 1.5, 2.0 and 2.5 W cm^{-2} for 10 min, the temperatures of Gd–Fe(7 : 3)–TA solution rose rapidly. ΔT (T_{max} − T_0) increased monotonically with the increase of laser power density (ΔT = 34.6 °C for 1.0 W cm^{-2}, 36.8 °C for 1.5 W cm^{-2}, 41.6 °C for 2.0 W cm^{-2}, and 45.7 °C for 2.5 W cm^{-2}). The photostability of Gd–Fe(7 : 3)–TA solution was further investigated. The Gd–Fe(7 : 3)–TA solution was exposed to four cycles of on/off NIR laser irradiation (808 nm, 1.0 W cm^{-2}, 10 min). The equilibrium temperature of Gd–Fe(7 : 3)–TA solution was nearly unchanged (Fig. 4d). The UV-vis spectra for Gd–Fe (7 : 3)–TA solution showed that the absorption of coordination

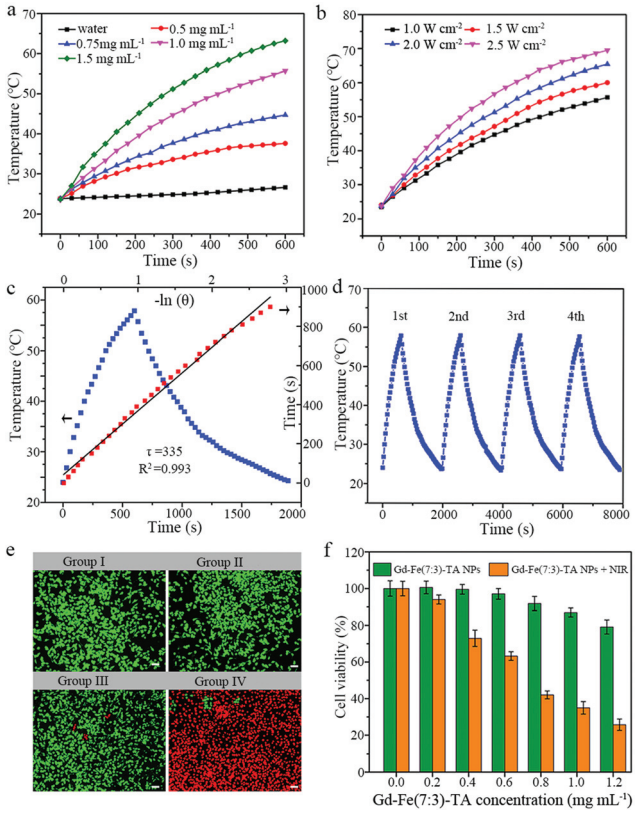

Fig. 4 (a) Time-dependent temperature change curves for Gd–Fe (7 : 3)–TA solution with different concentrations under an 808 nm laser at a power density of 1.0 W cm^{-2}. (b) Time-dependent temperature change curves for Gd–Fe(7 : 3)–TA solution (1.0 mg mL^{-1}) under laser irradiation with different power densities (1.0, 1.5, 2.0 and 2.5 W cm^{-2}). (c) The linear correlation of the cooling time *versus* negative natural logarithm of driving force temperature. (d) Temperature elevation curves of Gd–Fe(7 : 3)–TA solution over four cycles of 808 nm NIR laser on/off irradiation. (e) Confocal fluorescence images of HeLa cells after different treatments (group I, control; group II, Gd–Fe(7 : 3)–TA treatment; group III, 808 nm laser irradiation; group IV, Gd–Fe(7 : 3)–TA treatment plus 808 nm laser irradiation). The cells were co-stained with calcein acetoxymethyl ester (green, living cells) and propidium iodide (red, dead cells). Scale bar, 50 μm. (f) Relative photo (or dark) viabilities of HeLa cells after treatment with Gd–Fe(7 : 3)–TA at different concentrations with (or without) 808 nm NIR laser irradiation (1.0 W cm^{-2} for 5 min).

polymer solution was not changed obviously after four cycles of irradiation (Fig. S11a†). The hydrodynamic size of Gd–Fe (7 : 3)–TA after four cycles of irradiation was the same as the initial diameter, further indicating a good photostability of Gd–Fe(7 : 3)–TA (Fig. S11b†). The photothermal conversion efficiency (η) was calculated to be 37% according to the fitting cooling curve (Fig. 4c), which was higher than that of some photothermal agents reported before, such as that of Au nanorods (21%), $Cu_{2-x}Se$ (22%) and MoS_2 (34.46%).[58–60] The η was comparable to that of other iron–phenolic coordination polymers (Table S4†).

Encouraged by the above results, we further evaluate the feasibility of Gd–Fe(7 : 3)–TA as a PTT agent for cancer therapy. HeLa cells were used as a model cell. The experiments were divided into four groups: group I, control (cells without any treatment); group II, Gd–Fe(7 : 3)–TA treatment only; group III, 808 nm laser irradiation only; group IV, Gd–Fe(7 : 3)–TA treatment plus 808 nm laser irradiation. After treatment, the cells were stained with both calcein– AM and propidium iodide (PI). The cells in group I, group II and group III showed negligible cell death, whereas nearly all cells were killed in group IV (Fig. 4e). These results not only suggested the low cytotoxicity of Gd–Fe(7 : 3)–TA, but also demonstrated that Gd–Fe(7 : 3)–TA could effectively kill the HeLa cells through the photothermal effect. We further quantitatively evaluated their photothermal cytotoxicity on cancer cells using a MTT (3-(4,5-dimethylthiazol-2-yl)-2,5-diphenyltetrazolium bromide) assay (Fig. 4f). After 12 h of incubation with different concentrations of Gd–Fe(7 : 3)–TA, the cell viability of HeLa cells was slightly hindered. Even at the highest dose of Gd–Fe(7 : 3)–TA (1.2 mg mL^{-1}), cell viability still remained at approximately 80.1%. However, upon laser irradiation, the cell viability decreased significantly when the concentration of Gd–Fe(7 : 3)–TA increased. Less than 25.7% of HeLa cells remained alive at a concentration of 1.2 mg mL^{-1}. These findings further demonstrated that Gd–Fe(7 : 3)–TA showed great promise for PTT.

Inspired by its efficient photothermal performance *in vitro*, Gd–Fe(7 : 3)–TA was further used for PTT *in vivo*. The BALB/C mice bearing EMT-6 tumors were intravenously injected with Gd–Fe(7 : 3)–TA. At 4 h post-injection, the mice were exposed to an 808 nm laser at 1.0 W cm^{-2} for 5 min. The temperature of the tumor region increased to 52.4 °C after irradiation for 5 min (Fig. 5a and b). In contrast, the temperatures for the control group increased to 38.8 °C without injection of CPs, indicating that the Gd–Fe(7 : 3)–TA could act as an efficient photothermal agent to locally heat the tumor under 808 nm laser irradiation.

Tumor inhibition efficacy of Gd–Fe(7 : 3)–TA was evaluated by *in vivo* treatment of EMT-6 tumor-bearing mice. The mice were randomly divided into four groups (n = 5 per group) and treated with (a) phosphate buffer saline only (control group), (b) Gd–Fe(7 : 3)–TA nanoparticles only (NPs group), (c) 808 nm NIR only (laser group) and (d) Gd–Fe(7 : 3)–TA and 808 nm NIR laser (PTT group). During the treatment process, the body weight of mice in the four groups did not changed obviously, indicating the low systemic toxicity of the CPs and treatment type (Fig. 5c). The tumors in the PTT group were significantly reduced compared with the control, NP and laser groups (Fig. 5d and e), indicating that the Gd–Fe(7 : 3)–TA-mediated PTT can effectively inhibit tumor growth. The laser irradiation alone or Gd–Fe(7 : 3)–TA itself barely suppressed tumor growth. The histological analysis of tumors revealed that most of the tumor cells were damaged by PTT treatment. Conversely, tumor tissues from the control group that received Gd–Fe(7 : 3)–TA or laser only remained normal (Fig. 5f). The above results illustrated that Gd–Fe(7 : 3)–TA had significant PTT efficiency for anti-tumor treatment.

2.4. *In vivo* biodistribution and toxicology investigation

It is significant to understand the biodistribution, clearance and toxicology of the nanoscale CPs in biological systems. We

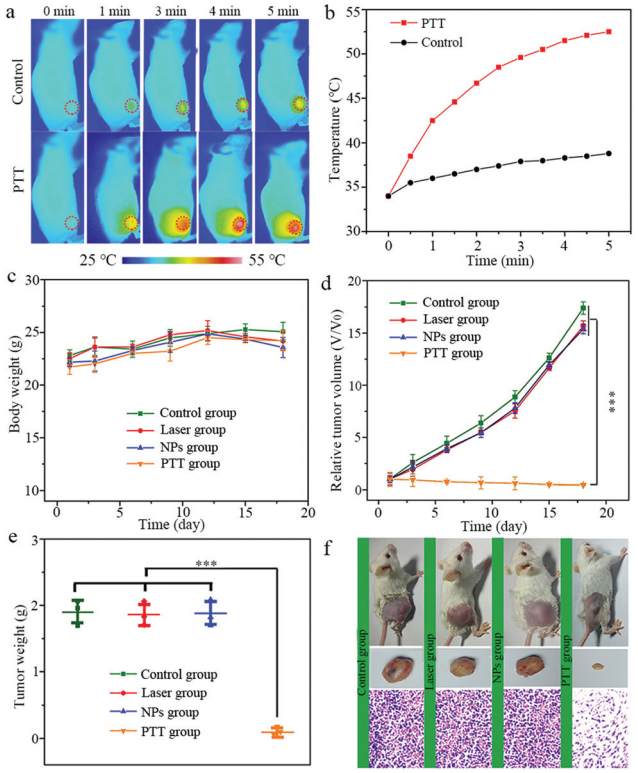

Fig. 5 (a) *In vivo* IR thermal images of tumor bearing mice injected with Gd–Fe(7 : 3)–TA or PBS upon laser irradiation for 5 min and (b) the corresponding temperature changes in the tumor region. (c) Body weight and (d) tumor volume curves of different groups of mice after intravenous injection. (e) The weight of tumors in mice sacrificed after 18-day observation. (f) Photograph of mice, tumor and H&E staining of tumor slides: from left to right: control group, laser group, NPs group and PTT group. Results are presented as mean ± S.D., (n = 5, *p < 0.05, **p < 0.01, ***p < 0.001, analyzed by Student's t-test).

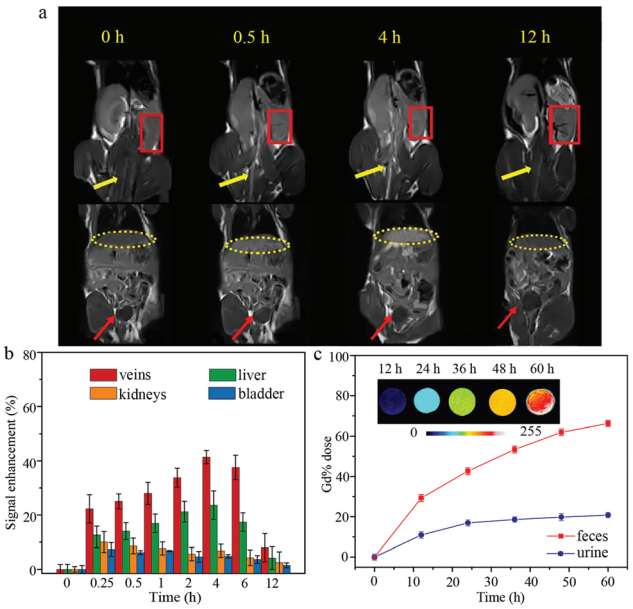

Fig. 6 (a) Representative MR images of a mouse at 0, 0.5, 4 and 12 h after intravenous injection. The yellow arrows, red arrows, red rectangles and yellow ellipses represent veins, bladder, kidneys and liver, respectively. (b) The dynamic signal enhancement of the regions including the kidneys, veins, liver and bladder at 0, 0.25, 0.5, 1, 2, 4, 6 and 12 h after intravenous injection of Gd–Fe(7 : 3)–TA. (c) Accumulative feces and urine excretion of Gd–Fe(7 : 3)–TA within 60 hours after intravenous injection. The inset shows MR images of accumulative feces at different time intervals.

employed *in vivo* MRI to investigate the biodistribution and clearance of Gd–Fe(7 : 3)–TA in mice. Gd–Fe(7 : 3)–TA solution was intravenously injected into the mice. T_1-Weighted MR images were acquired at 0, 0.25, 0.5, 1, 2, 4, 6 and 12 h after injection. The MR signal in vena cava enhanced rapidly over time and reached the maximum at 4 h (Fig. 6a and b, Fig. S12†), indicating that Gd–Fe(7 : 3)–TA nanoparticles were dispersed and circulated well in the bloodstream. An enhanced MR signal in the liver region was observed and the high signal states persisted for 4 hours, indicating that Gd–Fe(7 : 3)–TA nanoparticles mainly accumulated in the reticuloendothelial system organ. After 12 h, the signal in the liver region significantly reduced, suggesting that most of Gd–Fe(7 : 3)–TA could be effectively excreted out of the mice body by the hepatobiliary pathway.[61,62] In contrast, the signal in the kidneys and bladder showed a barely significant change throughout the course of the experiment, indicating that a small portion of Gd–Fe(7 : 3)–TA NPs were excreted from the mice body *via* renal filtration.

The contents of Gd in the main organs were measured by ICP-MS. At 24 h post-injection, Gd–Fe(7 : 3)–TA CPs were principally accumulated in livers and tumors (Fig. S13a†). The Gd was accumulated in the tumor after injection for 4 h. The Gd content in major organs declined gradually and nearly disappeared at 72 h post-injection. The biodistribution of Fe species in mice was similar to that of Gd species (Fig. S13b†).

The urine and feces of mice were collected during the experiment for ICP-MS and MRI measurements at different time intervals after intravenous injection of Gd–Fe(7 : 3)–TA. The accumulative urinary and fecal excretion within 60 hours after intravenous injection was 64.2% and 18.7% of the injected dose, respectively. Such results provide additional evidence of the hepatobiliary excretion pathway of the injected Gd–Fe(7 : 3)–TA. Correspondingly, the MRI signal of the feces increased continuously from 12 to 60 h (Fig. 6c). These results confirmed that Gd–Fe(7 : 3)–TA could be effectively excreted from the mice body through the hepatobiliary pathway, and thereby minimize long-term retention and potential toxicity.

Furthermore, *in vivo* toxicity of the Gd–Fe(7 : 3)–TA was examined with hematology and histochemical analyses. Compared with the control group, the hematology analysis indexes in the Gd–Fe(7 : 3)–TA treated groups on day 0, 1 and 3 post-injection were normal and well matched with the reference normal ranges (Fig. S14†).[63] A slight reduction was observed for the WBC level in the Gd–Fe(7 : 3)–TA-treated group on day 1 post-injection and fell into the normal range on day 3 post-injection, which were associated with the temporal iron overload in the body and the WBC level could recover once the CPs were cleared.[63,64] The major organs

(heart, liver, spleen, lungs and kidneys) of the Gd–Fe(7 : 3)–TA-treated mice were collected on day 0, 1 and 3 after injection for a histology analysis. Compared to the control group, neither apparent abnormalities nor lesions were observed in the organs of the Gd–Fe(7 : 3)–TA-treated mice (Fig. S15†). The preliminary toxicity experiment conducted in the mice body indicated that Gd–Fe(7 : 3)–TA may be used as a potential nanoplatform for biomedical applications.

3. Conclusion

In summary, Gd/Fe–bimetal–phenolic coordination polymer nanoparticles with a tunable molar ratio of Gd/Fe, an ultrasmall diameter (20–30 nm), and high dispersibility and stability were successfully synthesized *via* a controllable metal–catechol coordination assembly approach using plant polyphenols as an organic ligand, and Gd nitrate and ferrous sulphate as a metal source. The contents of Gd and Fe in the CPs can be easily tailored by changing the molar ratios of metal sources to tannic acid during the synthesis process. The obtained bimetal–phenolic coordination polymers showed composition-dependent performance for longitudinal relaxivity and photothermal conversion. The bimetal–phenolic coordination polymers with an optimized molar ratio of Gd/Fe can be used as an efficient contrast agent for *in vivo* MRI of mouse tumors. Moreover, they could also act as a PTT agent to effectively inhibit tumor growth. It is believed that this work would provide a reliable strategy to synthesize multifunctional coordination polymer nanoparticles for promising biomedical applications by tailoring the structure and compositions of nanoscale coordination polymers.

4. Experimental details

Experimental details are given in the ESI.†

Conflicts of interest

There are no conflicts to declare.

Acknowledgements

This work was financially supported by the National Natural Science Foundation of China (No. 21701130 and 311343), the Fundamental Research Funds for the Central Universities, and "Young Talent Support Plan" of Xi'an Jiaotong University. We thank Miss Jiao Li and Mr Zijun Ren at Instrument Analysis Center of Xi'an Jiaotong University for their assistance with TEM analysis.

References

1 D. Ni, W. Bu, E. B. Ehlerding, W. Cai and J. Shi, *Chem. Soc. Rev.*, 2017, **46**, 7438–7468.
2 E. Terreno, D. Delli Castelli, A. Viale and S. Aime, *Chem. Rev.*, 2010, **110**, 3019–3042.
3 S. Viswanathan, Z. Kovacs, K. N. Green, S. J. Ratnakar and A. D. Sherry, *Chem. Rev.*, 2010, **110**, 2960–3018.
4 P. Caravan, J. J. Ellison, T. J. McMurry and R. B. Lauffer, *Chem. Rev.*, 1999, **99**, 2293–2352.
5 J. Wahsner, E. M. Gale, A. Rodriguez-Rodriguez and P. Caravan, *Chem. Rev.*, 2019, **119**, 957–1057.
6 Y. Liu, Z. Yang, X. Huang, G. Yu, S. Wang, Z. Zhou, Z. Shen, W. Fan, Y. Liu, M. Davisson, H. Kalish, G. Niu, Z. Nie and X. Chen, *ACS Nano*, 2018, **12**, 8129–8137.
7 Z. Shen, J. Song, Z. Zhou, B. C. Yung, M. A. Aronova, Y. Li, Y. Dai, W. Fan, Y. Liu, Z. Li, H. Ruan, R. D. Leapman, L. Lin, G. Niu, X. Chen and A. Wu, *Adv. Mater.*, 2018, **30**, 1803163.
8 Q. Luo, X. Xiao, X. Dai, Z. Duan, D. Pan, H. Zhu, X. Li, L. Sun, K. Luo and Q. Gong, *ACS Appl. Mater. Interfaces*, 2018, **10**, 1575–1588.
9 S. Lu, X. Li, J. Zhang, C. Peng, M. Shen and X. Shi, *Adv. Sci.*, 2018, **5**, 1801612.
10 S. Aime, S. G. Crich, E. Gianolio, G. B. Giovenzana, L. Tei and E. Terreno, *Coord. Chem. Rev.*, 2006, **250**, 1562–1579.
11 Y. Liu, P. Bhattarai, Z. Dai and X. Chen, *Chem. Soc. Rev.*, 2019, **48**, 2053–2108.
12 A. Banerjee, V. Alves, T. Rondao, J. Sereno, A. Neves, M. Lino, A. Ribeiro, A. J. Abrunhosa and L. S. Ferreira, *Nanoscale*, 2019, **11**, 13243–13248.
13 S. Gai, G. Yang, P. Yang, F. He, J. Lin, D. Jin and B. Xing, *Nano Today*, 2018, **19**, 146–187.
14 K. Lu, T. Aung, N. Guo, R. Weichselbaum and W. Lin, *Adv. Mater.*, 2018, **30**, 1707634.
15 G. Lan, K. Ni and W. Lin, *Coord. Chem. Rev.*, 2019, **379**, 65–81.
16 Y. Yang, W. Zhu, L. Feng, Y. Chao, X. Yi, Z. Dong, K. Yang, W. Tan, Z. Liu and M. Chen, *Nano Lett.*, 2018, **18**, 6867–6875.
17 J. Liu, Q. Chen, W. Zhu, X. Yi, Y. Yang, Z. Dong and Z. Liu, *Adv. Funct. Mater.*, 2017, **27**, 1605926.
18 M. X. Wu and Y. W. Yang, *Adv. Mater.*, 2017, **29**, 1606134.
19 H. Ejima, J. J. Richardson and F. Caruso, *Nano Today*, 2017, **12**, 136–148.
20 M. A. Rahim, S. L. Kristufek, S. Pan, J. J. Richardson and F. Caruso, *Angew. Chem., Int. Ed.*, 2019, **58**, 1904–1927.
21 L. Q. Xu, K. Neoh and E. Kang, *Prog. Polym. Sci.*, 2018, **87**, 165–196.
22 S. Quideau, D. Douat-Casassus and L. Pouysgu, *Angew. Chem., Int. Ed.*, 2011, **50**, 586–621.
23 H. Ejima, J. J. Richardson, K. Liang, J. P. Best, M. P. V. Koeverden, G. K. Such, J. Cui and F. Caruso, *Science*, 2013, **341**, 154.
24 J. Guo, Y. Ping, H. Ejima, K. Alt, M. Meissner, J. J. Richardson, Y. Yan, K. Peter, D. von Elverfeldt, C. E. Hagemeyer and F. Caruso, *Angew. Chem., Int. Ed.*, 2014, **53**, 5546–5551.

25 J. Wei, Y. Liang, Y. Hu, B. Kong, J. Zhang, Q. Gu, Y. Tong, X. Wang, S. P. Jiang and H. Wang, *Angew. Chem., Int. Ed.*, 2016, **55**, 12470–12474.
26 J. Wei, Y. Liang, Y. Hu, B. Kong, G. P. Simon, J. Zhang, S. P. Jiang and H. Wang, *Angew. Chem., Int. Ed.*, 2016, **55**, 1355–1359.
27 C. Maerten, L. Lopez, P. Lupattelli, G. Rydzek, S. Pronkin, P. Schaaf, L. Jierry and F. Boulmedais, *Chem. Mater.*, 2017, **29**, 9668–9679.
28 X. Chen, Z. Yi, G. Chen, X. Ma, W. Su, X. Cui and X. Li, *J. Mater. Chem. B*, 2019, **7**, 4066–4078.
29 G. Wang, J. Qin, X. Zhou, Y. Deng, H. Wang, Y. Zhao and J. Wei, *Adv. Funct. Mater.*, 2018, **28**, 1806144.
30 J. Wei, G. Wang, F. Chen, M. Bai, Y. Liang, H. Wang, D. Zhao and Y. Zhao, *Angew. Chem., Int. Ed.*, 2018, **57**, 9838–9843.
31 W. Zhu, G. Xiang, J. Shang, J. Guo, B. Motevalli, P. Durfee, J. O. Agola, E. N. Coker and C. J. Brinker, *Adv. Funct. Mater.*, 2018, **28**, 1705274.
32 Y. Dai, Z. Yang, S. Cheng, Z. Wang, R. Zhang, G. Zhu, Z. Wang, B. C. Yung, R. Tian, O. Jacobson, C. Xu, Q. Ni, J. Song, X. Sun, G. Niu and X. Chen, *Adv. Mater.*, 2018, **30**, 1704877.
33 Y. Dai, J. Guo, T.-Y. Wang, Y. Ju, A. J. Mitchell, T. Bonnard, J. Cui, J. J. Richardson, C. E. Hagemeyer, K. Alt and F. Caruso, *Adv. Healthcare Mater.*, 2017, **6**, 1700467.
34 Y. Dai, S. Cheng, Z. Wang, R. Zhang, Z. Yang, J. Wang, B. C. Yung, Z. Wang, O. Jacobson, C. Xu, Q. Ni, G. Yu, Z. Zhou and X. Chen, *ACS Nano*, 2018, **12**, 455–463.
35 Z. Yang, Y. Dai, C. Yin, Q. Fan, W. Zhang, J. Song, G. Yu, W. Tang, W. Fan, B. C. Yung, J. Li, X. Li, X. Li, Y. Tang, W. Huang, J. Song and X. Chen, *Adv. Mater.*, 2018, **30**, 1707509.
36 C. Wang, H. Sang, Y. Wang, F. Zhu, X. Hu, X. Wang, X. Wang, Y. Li and Y. Cheng, *Nano Lett.*, 2018, **18**, 7045–7051.
37 H. Huang, J. Qin, G. Wang, Z. Guo, X. Yu, Y. Zhao and J. Wei, *CrystEngComm*, 2018, **20**, 7626–7630.
38 T. Liu, M. Zhang, W. Liu, X. Zeng, X. Song, X. Yang, X. Zhang and J. Feng, *ACS Nano*, 2018, **12**, 3917–3927.
39 F. Liu, X. He, H. Chen, J. Zhang, H. Zhang and Z. Wang, *Nat. Commun.*, 2015, **6**, 8003.
40 Q. Jin, W. Zhu, D. Jiang, R. Zhang, C. J. Kutyreff, J. W. Engle, P. Huang, W. Cai, Z. Liu and L. Cheng, *Nanoscale*, 2017, **9**, 12609–12617.
41 G. Zhao, H. Wu, R. Feng, D. Wang, P. Xu, P. Jiang, K. Yang, H. Wang, Z. Guo and Q. Chen, *ACS Appl. Mater. Interfaces*, 2018, **10**, 3295–3304.
42 Z. Dong, L. Feng, Y. Chao, Y. Hao, M. Chen, F. Gong, X. Han, R. Zhang, L. Cheng and Z. Liu, *Nano Lett.*, 2019, **19**, 805–815.
43 Y. Wang, J. Zhang, C. Zhang, B. Li, J. Wang, X. Zhang, D. Li and S.-K. Sun, *ACS Sustainable Chem. Eng.*, 2019, **7**, 994–1005.
44 P. Zhang, Y. Hou, J. Zeng, Y. Li, Z. Wang, R. Zhu, T. Ma and M. Gao, *Angew. Chem., Int. Ed.*, 2019, **58**, 11088–11096.
45 G. Wang, J. Qin, Y. Zhao and J. Wei, *J. Colloid Interface Sci.*, 2019, **544**, 241–248.
46 G. Wang, X. Zhou, J. Qin, Y. Liang, B. Feng, Y. Deng, Y. Zhao and J. Wei, *ACS Appl. Mater. Interfaces*, 2019, **11**, 35060–35067.
47 Y. Li, Y. Huang, Z. Wang, F. Carniato, Y. Xie, J. P. Patterson, M. P. Thompson, C. M. Andolina, T. B. Ditri, J. E. Millstone, J. S. Figueroa, J. D. Rinehart, M. Scadeng, M. Botta and N. C. Gianneschi, *Small*, 2016, **12**, 668–677.
48 R. K. Feller and A. K. Cheetham, *Solid State Sci.*, 2006, **8**, 1121–1125.
49 S. Suárez-García, N. Arias-Ramos, C. Frias, A. P. Candiota, C. Arús, J. Lorenzo, D. Ruiz-Molina and F. Novio, *ACS Appl. Mater. Interfaces*, 2018, **10**, 38819–38832.
50 M. Borges, S. Yu, A. Laromaine, A. Roig, S. Suárez-García, J. Lorenzo, D. Ruiz-Molinaa and F. Novio, *RSC Adv.*, 2015, **5**, 86779–86783.
51 W. S. Li, J. Luo and Z. N. Chen, *Inorg. Chem. Commun.*, 2011, **14**, 1898–1900.
52 M. Liu, C. Cai, J. Li, J. Zhao, W. Teng and R. Liu, *J. Colloid Interface Sci.*, 2018, **528**, 1–9.
53 Z. Fu and R. Chen, *J. Anal. Methods Chem.*, 2019, **2019**, 3894571.
54 D. Raiser and J. P. Deville, *J. Electron Spectrosc. Relat. Phenom.*, 1991, **57**, 91–97.
55 A. P. Grosvenor, B. A. Kobe, M. C. Biesinger and N. S. McIntyre, *Surf. Interface Anal.*, 2004, **36**, 1564–1574.
56 N. R. Perron, H. C. Wang, S. N. DeGuire, M. Jenkins, M. Lawson and J. L. Brumaghim, *Dalton Trans.*, 2010, **39**, 9982–9987.
57 H. Lee, W. I. Kim, W. Youn, T. Park, S. Lee, T.-S. Kim, J. F. Mano and I. S. Choi, *Adv. Mater.*, 2018, **30**, 1805091.
58 Z. Li, H. Huang, S. Tang, Y. Li, X.-F. Yu, H. Wang, P. Li, Z. Sun, H. Zhang, C. Liu and P. K. Chu, *Biomaterials*, 2016, **74**, 144–154.
59 L. Tan, S. Wang, K. Xu, T. Liu, P. Liang, M. Niu, C. Fu, H. Shao, J. Yu, T. Ma, X. Ren, H. Li, J. Dou, J. Ren and X. Meng, *Small*, 2016, **12**, 2046–2055.
60 C. M. Hessel, V. P. Pattani, M. Rasch, M. G. Panthani, B. Koo, J. W. Tunnell and B. Korgel, *Nano Lett.*, 2011, **11**, 2560–2566.
61 J. Bai, X. Jia, W. Zhen, W. Cheng and X. Jiang, *J. Am. Chem. Soc.*, 2018, **140**, 106–109.
62 C. Xu, Y. Wang, H. Yu, H. Tian and X. Chen, *ACS Nano*, 2018, **12**, 8255–8265.
63 K. Yang, J. Wan, S. Zhang, Y. Zhang, S. T. Lee and Z. Liu, *ACS Nano*, 2011, **5**, 516–522.
64 J. Han, G. Liang and D. Xing, *Chem. – Eur. J.*, 2019, **25**, 8353–8362.